Thermal expansion of CuInSe$_2$ in the 11–1,073 K range: an X-ray diffraction study

**W. Paszkowicz · R. Minikayev · P. Piszora ·
D. Trots · M. Knapp · T. Wojciechowski ·
R. Bacewicz**

Abstract Structural and elastic properties of chalcopyrite-type CuInSe$_2$ are determined in almost full stability range of temperature from 11 to 1,073 K, by in situ X-ray diffraction, employing a synchrotron-radiation source. The studied polycrystalline sample was prepared from a stoichiometric single crystal. Phase analysis reveals the formation of a trace amount of indium oxide impurity phase at the highest temperatures studied. From the obtained smooth lattice-parameter dependencies on temperature, the temperature dependencies of thermal expansion coefficients are derived. These coefficients are found to follow the trends previously reported for narrow temperature intervals. The present results provide a clear experimental evidence that the linear expansion coefficient is slightly negative below 47 K in both, a and c, directions; this temperature limit is in between the previously reported theoretical value (35 K) and the experimental ones (60 and 80 K) of such limit.

W. Paszkowicz (✉) · R. Minikayev · T. Wojciechowski
Institute of Physics PAS, al. Lotników 32/46, 02-668 Warsaw,
Poland
e-mail: paszk@ifpan.edu.pl

P. Piszora
Faculty of Chemistry, A. Mickiewicz University,
ul. Grunwaldzka 6, 60-780 Poznan, Poland

D. Trots
Bayerisches Geoinstitut, Universität Bayreuth,
Universitätsstraße 30, 95447 Bayreuth, Germany

M. Knapp
Karlsruhe Institute of Technology, Institute for Applied
Materials-Energy Storage Systems, Karlsruhe, Germany

R. Bacewicz
Faculty of Physics, Warsaw University of Technology,
ul. Koszykowa 75, 00-662 Warsaw, Poland

1 Introduction

Copper indium diselenide, CuInSe$_2$ (CIS), is one of the ternary compounds occurring in the CuSe$_2$–In$_2$Se$_3$ phase diagram [1, 2]. This material is widely studied, due mainly to its applicability as ultrathin efficient absorber in solar cells [3]. The reported energy-conversion efficiency approaches 20 % [3–7]. In polycrystalline films, the efficiency may be affected by the size and orientation of crystallites [8]. CIS is considered as a material of performance not degrading with time [9]. However, in a recent study it was found that some degradation, followed by passivation, takes place at room temperature (RT) at the surface, one of the degradation products being the indium oxide [10]. CIS can also have other applications as a component of photovoltaic detectors [11] and of microscopic diodes [12]. Nanocrystalline (wurtzite-type) CIS has been proposed for use as a material for high-efficiency visible light or ultraviolet photodetectors [13].

CuInSe$_2$ crystallizes in the tetragonal chalcopyrite (CuFeS$_2$)-type structure, space group $I\bar{4}2d$), related to the zincblende structure type. In the chalcopyrite structure, the c axis is approximately twice as long as compared to the basic zincblende cell, and the deviation of the reduced axial ratio $\eta = c/(2a)$ from 1 is connected with the so-called tetragonal distortion. (In considerations of CIS and other chalcopyrite-type compounds, the tetragonal distortion defined as $1 - \eta$ is frequently used.) When surveying the structural data for CuInSe$_2$, we noticed a considerable scatter of the reported a and c values. One of possible reasons of this scatter is deviation from stoichiometry.

The chalcopyrite-type CuInSe$_2$ is known to exist in a composition range (as noticed in [14]). The samples with a copper deficit and with a deviation from ideal Se content

have been studied in [15] and [16], respectively. Off-stoichiometric samples have also been studied, e.g. in [17] providing, in particular, the structural information in the low-temperature range. In Refs. [18, 19] some off-stoichiometry effect on microstructure and structure has been shown. Apart of the classical X-ray diffraction, the neutron diffraction has proven to be useful in such investigations [20]. The occurrence of a considerable range of CuInSe$_2$ off-stoichiometry is attributed to remarkably low formation enthalpy of defect pairs [21]. The deviations from stoichiometry in crystals prepared at various conditions lead to a large spread of physical properties of the material [22].

CuInSe$_2$ undergoes a phase transition to $F\bar{4}3m$ zincblende-type phase at 1,083 K [9], or at 1,079 K with a small hysteresis of 10 K [23]; the zincblende phase can occur as a metastable one in thin films [24]. The above-mentioned metastable wurtzite-type polymorph has been occasionally reported for CIS nanocrystals [25].

Early studies on the thermal behavior of the lattice parameters of CuInSe$_2$, usually based on X-ray diffraction, have covered limited temperature ranges: 301–839 K [26], 30–300 K [27]), 85–650 K [28] and 295–723 K [29] with typically a low number of experimental points; the most recent study [23] has been focused on the vicinity of the high-temperature tetragonal–cubic phase transition.

The earliest studies of thermal expansion of CuInSe$_2$ employed dilatometric and related methods (as summarized in [30]) yielding only the linear expansion coefficient α_L in the high-temperature range; its value at RT exhibited a considerable scatter between 5.8 and 9.1 MK^{-1}. Early X-ray studies on thermal behavior of lattice parameters of CuInSe$_2$, typically based on the lattice-parameter data, have been limited to specific temperatures of 301–839 K (six experimental points) [26]) 30–300 K [27], 85–650 K [28], 295–723 K [29]. In the only study focused on the low-temperature range [27], the dependencies for (001) and (011) oriented single crystals have been measured, the result for $c(T)$ being derived from these two curves. In the cited paper, it has been found that the minima at $a(T)$ and $c(T)$ are at different temperatures (60 and 80 K), thermal expansion coefficient (TEC) thus being negative below 60 K (direction a) or below 80 K (direction c) and steeply increasing with temperature up to 400 K. The TEC values at 300 K reported by several groups are generally consistent within $\sim$ 10 %.

Little is known on the structural changes with temperature, from the theoretical point of view. Semi-empirical estimations of the thermal expansion at RT have been reported in [31] and [32]. The former result is quite consistent with experimental values. In [33], an average linear thermal expansion dependence on temperature has been

calculated; the results show that the TEC becomes negative below about 35 K; the absolute TEC values are found to be much larger as compared to all experiments.

Due to limited temperature ranges and lattice-parameter accuracy as well as to a low number of experimental points, the existing experimental results do not present a consistent image of the structural and elastic properties of CIS as a function of temperature.

As mentioned above, previous studies did not cover the full temperature range of the chalcopyrite-type CuInSe$_2$. The present study shows the experimentally determined low- and high-temperature (LT/HT) thermal expansion of CuInSe$_2$. The experimental approach is based on in situ X-ray powder diffraction measurements, using synchrotron radiation. Consequently, the complete stability range of this compound is now covered with reliability ascertained by careful on-line calibration. The unit cell dimensions and TEC for CuInSe$_2$ are determined in the 11–1,073 K temperature range; the obtained results are discussed on the ground of earlier reported data.

2 Experimental setup

The material used in the present study was a CuInSe$_2$ single crystal grown by the vertical Bridgman–Stockbarger method without seed from a stoichiometric amount of 5.5 N purity components. The ingot was melted and then held at 1,313 K for 5 h. Subsequently, it was moved at low speed through the hot zone of 1,403 K exhibiting a gradient of 2.5 K/cm, then cooled from 1,353 K down to 1,023 K at 1 K/h (slow cooling was applied because of the above-mentioned phase transformation at 1,079 K), then down to 773 K at 5 K/h and then quickly cooled to room temperature (for details, see [34, 35]). The copper-to-indium ratio in the crystal was verified with the *Bruker QUANTAX 400* EDS system attached to a scanning electron microscope; the result based on six randomly selected points of the surface is 0.996(11).

The fine CuInSe$_2$ powder was prepared for the powder diffraction experiments by grinding the single crystal in an agate mortar. For the non-ambient temperature experiments, a mixture of the powdered sample with a diamond powder was loaded into a 0.8-mm-diameter glass capillary (Hilgenberg) in the LT case and into a 0.3-mm-diameter quartz capillary (Hilgenberg) in the HT case. The capillaries were sealed in air.

The low- and high-temperature X-ray diffraction measurements were carried out with the powder diffractometer at the B2 bending-magnet beamline (at DORIS III ring, Hasylab/DESY) [36]. For both ranges, a Debye–Scherrer parallel beam geometry and the same on-line wavelength calibration method were used. The beam spot size was

1×15 mm^2 in the LT case and 1×4 mm^2 in the HT case; this selection allowed for optimizing the resolution and counting statistics.

The high-resolution experimental setup configuration adopted in the low-temperature region involved a He-closed-cycle cryostat allowing capillary rotation and a scintillation counter with analyzer crystal. The temperature stability and accuracy were better than 0.5 K. At high temperatures, the medium resolution setting with the OBI position-sensitive detector was used [37]. The patterns were recorded in the 2θ range from 5° to 45° with a step of 0.004°. The wavelengths used in the LT and HT ranges were $\lambda \cong 1.13363$ and 0.494974 Å, respectively. For elimination of the possible effect of wavelength fluctuations during the diffraction measurement, a diamond powder (Sigma-Aldrich #48,359-1 synthetic powder, of ~ 1 μm monocrystalline grain size and purity of 99.9 %) was used as internal wavelength calibrant, as proposed and applied in [38, 39]. The temperature lattice-parameter variation, $a(T)$, for diamond was deduced from the polynomial given in [40] (LT part) and from Ref. [16] cited in [41] (HT part) and slightly rescaled on the basis of a measurement of a mixture of diamond with silicon (NIST SRM640c) at 301 K, namely from 3.566879 [40] to 3.567350 Å.

The low-temperature experiment consisted of a data collection in a narrow angular range including the neighboring 228 and 424 CuInSe$_2$ peaks, preceded and followed by scans of the 220 diamond line. The average position of the diamond peak determined from the two mentioned scans served for wavelength calibration at each temperature. The applied 2θ step was 0.005°. Small temperature steps were intentionally used to verify the earlier reported existence and location of the minima in the lattice-parameter temperature dependencies. The measurements started from 11.2 K with steps of 4–10 K (run 1). The lattice parameters in the low-temperature range were derived from the fitted positions of the mentioned 228 and 424 reflections. The peak positions were determined by a Pearson-VII-profile fitting.

The high-temperature run 2 started at 301 K, then the measurement continued, beginning from 323 with 50 K steps up to 1,073 K, i.e. to the near vicinity of the phase transition point located at $\sim 1,080$ K. In this run, for the structural analysis in the high-temperature domain, Rietveld refinement was used employing the refinement program Fullprof.2 k v.5.30 [42].

3 Results and discussion

3.1 Structure of CuInSe$_2$ at ambient temperature

The diffraction data collected at temperature of 301 K with good statistics of about 150,000 counts at maximum do not show any trace of foreign phases in the powdered crystal. Rietveld refinement was performed using a model based on the chalcopyrite-type structure. The structural model for the refinement at 301 K data was built for the phase mixture of chalcopyrite, and diamond standard. A pseudo-Voigt profile-shape function was assumed in calculations. In the refinements, the background was manually determined. The following parameters were refined. For CuInSe$_2$: lattice parameters (2 parameters), free positional parameter of Se atom (1), scale factor (1), peak shape and width parameters (5), isotropic atomic displacement parameters (3) (total 12). The preferred orientation parameters were not refined because the tests showed that modeling the preferred orientation does not lead to improvement of the refinement quality factors. For diamond: scale factor (1), peak shape and width parameters (5), isotropic atomic displacement parameter (1) (total 7). Two instrumental parameters were fitted: systematic line-shift parameter and wavelength (total 2), whereas the lattice parameter of the standard was fixed during refinement at a value, a_{diam}, specific for a given temperature. The refinement provided the following structural parameters: $a = 5.78213(6)$ Å, $c = 11.6184(2)$ Å, $\eta = 1.00468(3)$, $V = 388.44(1)$ Å^3, $x_{\text{Se}} = 0.2250(5)$. Figure 1a documents that only reflections belonging to CuInSe$_2$ appear.

The above-listed ambient temperature lattice parameters of the studied sample are, in general, consistent with a significant number of literature data given in four tables. Table 1 presents the structural data of monocrystalline CuInSe$_2$ [29, 43–46], Table 2 shows data obtained by powder diffraction structure refinement using Rietveld or Le Bail method [15, 23, 47–54], Table 3 provides data obtained by powder and single crystal diffraction using traditional methods [16, 27, 28, 55, 56] and Table 4 provides data for thin films and nanocrystals [57–63]; more data for comparison can be found in [15, 48, 64] (in the last reference, theoretical values have also been considered). In Fig. 2, lattice parameters quoted in the tables are visualized. The figure shows numerous data for (nominally) stoichiometric samples. The opportunity of CuInSe$_2$ for existence at off-stoichiometric compositions is well known. To illustrate the variation due to deviation from stoichiometry, three reported datasets for nonstoichiometric ones are shown in Fig. 2, using distinct symbols.

Inspection of the figure leads to the following observations:

(a) For nominally stoichiometric samples:

- For multiple data points, alignment along the line corresponding to $\eta = 1.0047$ is observed. Experimental points are predominantly scattered along the line, in between the lines corresponding to $\eta = 1.0037$ and 1.0057.
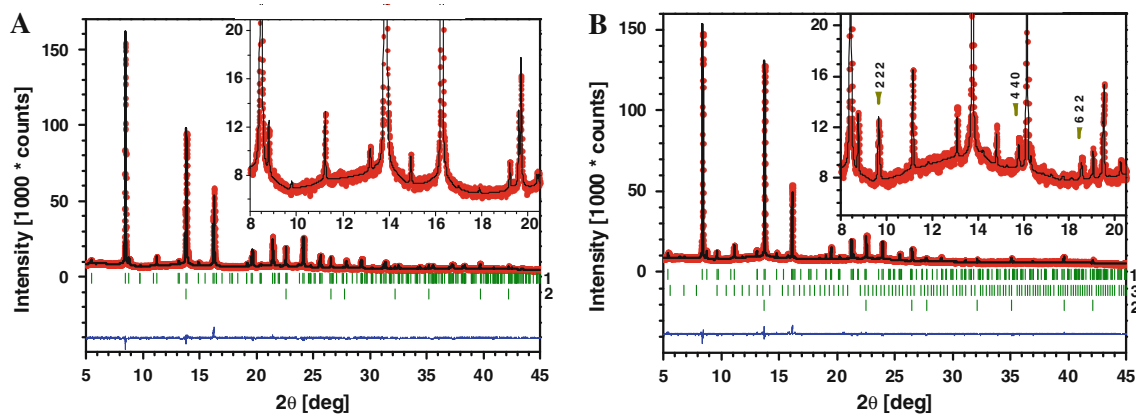
Fig. 1 Rietveld refinement result for CuInSe$_2$ for 301 (**a**) and 1,023 K (**b**). Reflection positions are indicated by *bars below* the diffraction curve. The reflection sets for the refined phases are identified by *numbers at the right axes*: CuInSe$_2$ (*1*), diamond (*2*), In$_2$O$_3$ (*3*). The *arrows in the inset in* **b** refer to indium oxide

Table 1 Room-temperature (RT) structural data of monocrystalline CuInSe$_2$, as obtained by single crystal structure refinement at classical and synchrotron instruments

a (Å)	c (Å)	Reduced axial ratio, η	V (Å^3)	Anion positional parameter, x_{Se}	T (K)	Crystal growth details	Ref.
Data from classical X-ray sources (set 1)							
5.7810(8)	11.6103(32)	1.0042(3)	388.02(18)	0.2258(3)	RT	Single crystal	[43]
5.7852(1)	11.6254(4)	1.00475(5)	389.09(3)	0.2252(2)	298	Single crystal (traveling heater method)	[44]
5.7855(4)	11.627(1)	1.0048(2)	389.18(9)	0.2268(1)	298	Single crystal (traveling heater method)	[44]
5.760(4)	11.591(7)	1.006(1)	384.56(37)	0.2305(7)	295	Single crystal	[29]
5.783(1)	11.621(1)	1.0048(3)	388.64(17)	n.r.	RT	Single crystal	[45]
Data from synchrotron sources (set 2)							
5.7877(44)	11.6274(59)	1.0045(82)	389(6)	0.22705(2)	RT	Single crystal (traveling heater method). No twinning, *p*-type crystal	[46]
5.7955(17)	11.6464(10)	1.0048(4)	391.18(26)	0.22714(2)	RT	Single crystal (traveling heater method). No twinning, *n*-type crystal	[46]
5.789(3)	11.639(3)	1.0053(7)	390.05(50)	0.2409(7)	RT	Single crystal (traveling heater method). No twinning, *n* + *p* type crystal	[46]

- Multiple literature data are located in a small area in the vicinity of the point $(a_1, c_1) = (5.782\ \text{Å}, 11.618\ \text{Å})$. Namely, ten data points are grouped close to the lower left corner in the area denoted by Ω (shown in the inset). This domain is defined through the following inequalities:

$$5.781\,\text{Å} < a < 5.784\,\text{Å} \tag{1}$$

$$11.616\,\text{Å} < c < 11.623\,\text{Å} \tag{2}$$

with arbitrarily chosen limits.
- The present data point is located within the Ω domain and at the mentioned line.
- The collected η values for thin films and nanocrystals typically deviate from the "ideal" value of 1.0047. More such data can be found in literature. For example, the data reported in [65]

(not plotted here) for polycrystalline thin films exhibit η values much differing from 1.0047.

The above comparative analysis of lattice parameters, supported by the scanning electron microscope result quoted in the beginning of Sect. 2, permits to conclude that the present sample is nearly stoichiometric.

(b) For nonstoichiometric samples:

- Three sets of data for nonstoichiometric CuInSe$_2$ plotted in Fig. 2 show a tendency to be arranged nearly in parallel with the lines of constant η.
- One (that reported in [16]) of the three sets is fully situated within the Ω domain, and another one (from [15]) is located there partially. Only the set quoted in [17] is outside Ω. It is worth noting that

Table 2 Room-temperature (RT) structural data of polycrystalline CuInSe$_2$, as obtained by powder diffraction structure refinement using Rietveld (PDR) or Le Bail method (PDL)

a (Å)	c (Å)	Reduced axial ratio, η	V (Å^3)	Anion positional parameter, x_{Se}	T (K)	Experiment	Crystal growth details	Ref.
Data from classical X-ray sources and neutron sources (set 3)								
5.7820(1)	11.6217(4)	1.00499	388.531	0.2267(7)	RT	PDR	SSR[a]	[15]
5.7876(1)	11.6296(4)	1.00470(5)	389.55(3)	0.2254	RT	PDR		[47]
5.78145(1)	11.61879(4)	1.00483(1)	388.360(3)	0.2271(4)	294	PDR	Powdered single crystal	[48]
5.7875	11.6295	1.00471	389.53(2)	0.22713	RT	PDR		[49]
5.7842(1)	11.6266(3)	1.00503(4)	388.99(2)	NR	RT	PDR	SSR	[50]
5.78361(8)	11.6214(3)	1.00468(4)	388.74(2)	0.22738(10)	RT	PDL, SCS*	SSR	[51]
5.7843(1)	11.6256(3)	1.00493(4)	388.97(2)	0.2296(3)	RT	PDR + NDR	SSR	[52]
–	–	1.004863	–	0.2297	RT	NDR	SSR	[20]
5.78505(4)	11.6231(1)	1.00458(4)	388.988(5)	0.2294(3)	RT	PDR + NDR	SSR	[53]
Data from synchrotron sources (set 4)								
5.79963(4)	11.6570(1)	1.00497		0.222(2)	295	SPDR	Powdered single crystal	[54]
5.8011(1)	11.6562(2)	1.00470(3)	392.26(2)	0.2270(5)	314	SPDR	SSR	[23]
Data from synchrotron sources with internal calibration (set 5)								
5.78213(6)	11.6184(2)	1.00468(3)	388.44(1)	0.2250(5)	301	SPDRIC	Powdered single crystal	This work[b]

PDR, SPDR, SPDRIC, X-ray powder diffraction, structure refinement using the Rietveld method for data collected at synchrotron sources (SPDR), and at synchrotron sources with internal wavelength calibration (SPDRIC); PDL, powder diffraction unit cell size refinement using the Le Bail method for data collected at laboratory source; NDR, neutron powder diffraction structure refinement using the Rietveld method; NR, not reported; SCS, single crystal structure refinement; SSR, solid-state reaction

* a and c from PDL, structure from SCS

[a] Data of the sample A3 (a representative of multiple samples) is quoted

[b] The fitting curve gives $a = 5.78229$ Å, $c = 11.61906$ Å, $\eta = 1.00471$ Å, $V = 388.48$ Å^3

Table 3 (set 6) Room-temperature (RT) structural data of CuInSe$_2$, as obtained using methods different than those of Tables 1 and 2

a (Å)	c (Å)	η	V (Å^3)	Anion positional parameter, x_{Se}	T (K)	Method	Material	Ref.
5.782(1)	11.620(1)	1.0048(3)	388.47(17)	0.235(5)	RT	AII	Polycrystal	[55]
5.7815(2)	11.6221(11)	1.0051(1)	388.48(6)		298	Single reflections	Single crystal	[27]
5.7821	11.6189	1.00473	388.45		RT		Polycrystal	[28]
5.7824	11.6192	1.00470	388.5	Not refined	RT		Polycrystal	[56]
5.7818	11.6173	1.00464	388.36		RT	Single reflections	Polycrystal	[16]

AII analysis of integrated intensities

the points representing the samples, in sets of [15, 16], the nearest to stoichiometric ones are located in a close vicinity of the present result (indicated by the arrows in Fig. 2).

- The strongly nonstoichiometric crystals can fall outside the lattice-parameter ranges shown in Fig. 2. For example, the points corresponding to a Cu-deficient crystal reported in [66] [$a = 5.730(5)$ Å, $c = 11.513(7)$ Å, $\eta = 1.0046(15)$, $x_{Se} = 0.2277(1)$, and $a = 5.731(5)$ Å, $c = 11.517(9)$ Å, $\eta = 1.0048(17)$, $x_{Se} = 0.2276(1)$] are located outside the figure.

In order to complete the discussion on non-stoichiometry, it is also worth adding that using the neutron diffraction instead of X-ray diffraction may lead to a better knowledge of crystal structure details such as deviation from stoichiometry. For CIS, a recent neutron diffraction study shows that, when moving with Cu:In ratio from 0.940 to 1.038, the η value increases from 1.00480 to 1.00485 and the anion

Table 4 (set 7) Room-temperature (RT) structural data for thin films and nanocrystals of CuInSe$_2$, as obtained by powder diffraction (PD) and other techniques

a (Å)	c (Å)	η	V (Å^3)	Anion positional parameter, x	T (K)	Method	Crystal growth details	Ref.
5.7810(13)	11.6422(26)	1.0069(5)	389.08(26)	0.2260(2)		SCR	Single crystal wafer	[57]
5.790	11.572	0.9993	387.94	0.226	RT	GID LSR	Thin film	[58]
5.7759(1)	11.5950(1)	1.00350(3)	386.82(2)	0.2232(1)	RT	PDR	Mechanical alloying	[59]
5.78	11.61	1.004	387.87	–	RT	PD	Nanoparticles	[60]
5.76	11.61	1.008	385.19	–	RT	PD	Nanoplates	[60]
5.787(3)	11.617(1)	1.004(1)	389.05(44)	–	RT	PD	Nanocrystal	[61]
5.774	11.603	1.00476	386.83	–	RT	GPDR	Thin films	[62]
5.816	11.464	0.986	387.78	–	RT	PDR	Mechanically alloyed, strained, 5 nm nanocrystals	[63]

Structure refinement using Rietveld method, or least squares refinement or single crystal data refinement is denoted by PDR and LSR, respectively. For Rietveld refinement of grazing incidence diffraction data abbreviation GPDR is used
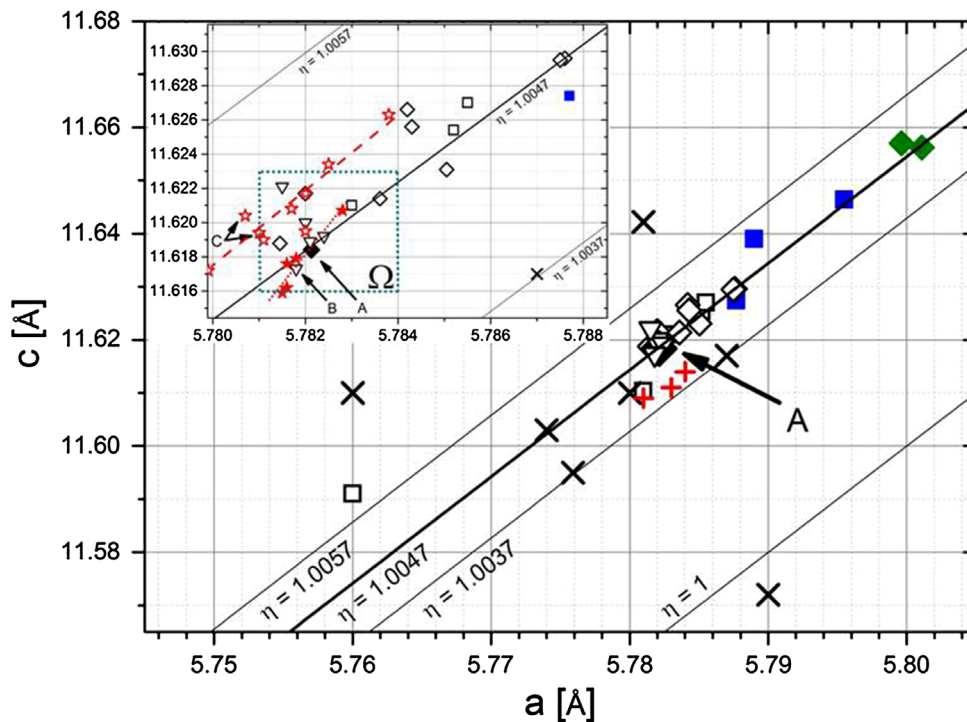
GID grazing incidence diffraction

Fig. 2 Correlation pattern for room-temperature a and c lattice parameters. Seven data sets listed in Tables 1, 2, 3 and 4 are displayed. In the *inset*, ten data points belonging to sets 1, 3, 5 and 6 (1, 3, 1 and 5 points, respectively) are grouped in the Ω area close to the *lower left inset corner* (limited by the *dotted rectangle*). The *thick solid line* represents the η value of 1.0047, the *thin lines* represent the ratios of 1, 1.0037 and 1.0057. *Open squares* single crystal, laboratory data (set 1), *filled squares* single crystal, synchrotron data (set 2), *open diamond* polycrystal, laboratory data (set 3), *small size filled diamond* polycrystal, synchrotron data (set 4), *large size filled diamond* polycrystal, internally calibrated synchrotron data (set 5), *open inverted triangle* single crystal or polycrystal synchrotron data (no structure refinement) (set 6), *cross symbol* data for thin films and nanocrystals (set 7), and *plus symbol* data for nonstoichiometric crystals [17]. For references—see Tables 1, 2, 3 and 4. The *inset* is completed by the nonstoichiometric samples data of [16] (*filled star*) with a nonstoichiometric selenium content and [15] (*open stars*) with a deficit of copper. The *arrows* indicate the present data (A), the sample from [16] with ideal Se content (B) and samples of Merino et al. [15] (C) close to the stoichiometric one (i.e. with a relatively small deficit of Cu)

positional parameter increases from 0.2281 to 0.2308 [20]. These values lead, through interpolation of the reported graphical data, to $\eta = 1.00486$ and $x_{Se} = 0.2297$ for the Cu:In ratio equal to 1. The changes in the η value in a broad composition range are thus quite small. This finding is consistent with the results of [18], where a marginal level of changes in η with varying composition has been observed.

3.2 Phase relationships at high temperatures and formation of a trace amount of In₂O₃ at $T \geq 683$ K

The structural model for the refinement of high-temperature data was the same as for 301 K, except that where needed it was completed by indium oxide. For the cases where cubic In₂O₃ was detected, the lattice parameter (1), scale factor (1), peak shape and width parameters (3) (total 5) were also refined for this phase. The trace In₂O₃ secondary phase could be studied owing to excellent counting statistics.

At temperatures ranging up to 623 K, the studied sample does not include any foreign phases. In the 673–1,023 K range, a trace amount of cubic In₂O₃ was observed with a relative peak height ratio increasing from 2 % at 673 K to 6 % at 773 and 823 K and then decreasing to 3 % at 1,023 K. An example of a Rietveld refinement for 1,023 K, assuming the model including the oxide, is displayed in Fig. 1b. As mentioned in the Introduction, this oxide is a degradation product of CIS photovoltaic films. It is therefore of interest to consider the presence and properties of the In₂O₃ minority phase in detail.

The lattice parameter of the impurity indium oxide is found to vary with temperature in a way agreeing with that determined by X-ray powder diffraction for a pure oxide powder sample [67] in the range 303–1,241 K (see Fig. 3):

$$a(T) = a_0[1 + A(T - 273) + B(T - 273)^2] \quad (3)$$

where the temperature is expressed in K, a_0 and $a(T)$ are the lattice-parameter values at 273 K (the value of 10.1175 Å) and at T, and A and B are coefficients equal to $7.20(6) \times 10^{-6}$ and $1.15(8) \times 10^{-9}$, respectively.

The crystal structure of In₂O₃ is known to depend on the crystallite size: for a small size, the corundum-type structure may form [68]. The crystallite size, D, of cubic In₂O₃ was evaluated for our sample on the basis of Scherrer formula. The size varies linearly with temperature between 15 and 30 nm (see Fig. 4) meaning that the crystallites tend to grow with increasing temperature. No trace of the corundum-type phase was found.

The observation, in the above-specified temperature range, of the In₂O₃ impurity phase for the studied sample is consistent with literature data on interaction of CuInSe₂ and related compounds with oxygen, observed in bulk material and in thin films.
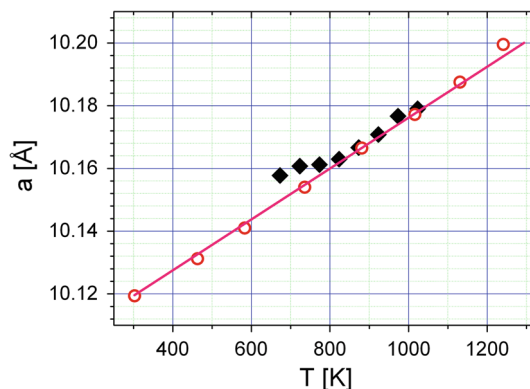

Fig. 3 Lattice parameter of In₂O₃ impurity phase as a function of temperature. *Filled diamonds* powdered single crystal (this work), *open circles* and *solid line* data of Kundra and Ali [67] for In₂O₃ polycrystal
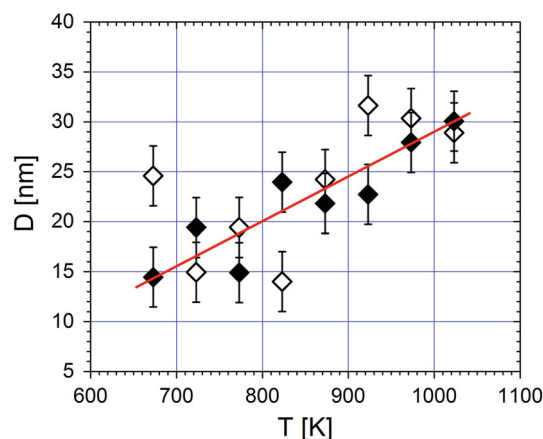

Fig. 4 The In₂O₃ crystallite size, D, was evaluated on the basis of Scherrer formula from the breadth of 440 (*open diamonds*) and 622 (*filled diamonds*) reflections. The *line* is a guide to eye. The larger scatter at lower temperatures is attributed to low peak intensity due to small oxide content at these temperatures

A native oxide in CuInSe₂ has been reported in Ref. [69]. Oxidation has also been reported in a related material, CuInS₂ [70]. In₂O₃ has been observed in CuInSe₂ oxidized at 373 K [71]. In₂O₃ and traces of CuO formed on CuInSe₂ during oxidation at 573–883 K have been studied in [72]. Oxidation at high temperatures has been observed also in [73]; it has been concluded on the basis of the cited study and literature data that the secondary phase appearing after oxidation may depend on the off-stoichiometry of the studied material. Appearance of In₂O₃ has been observed for an oxidized CuInSe₂ single crystal [74]. According to [75], at a low oxygen pressure the oxide does not form.

It is noteworthy that studies of thin films have shown that heating of CuInSe₂ in the presence of oxygen produces In₂O₃ and (volatile) SeO₂ already in the 423–573 K range [76]. Cu_xSe and Cu₂Se may be formed at high temperatures

Table 5 Temperature range for indium oxide observation in the oxidation processes of CuInSe$_2$

Oxidized material	In$_2$O$_3$ observation range (K)	Ref.
CuInSe$_2$ crystals and films	423–573	[76]
CuInSe$_2$ crystal (thickness < 60 nm)	373	[71]
CuInSe$_2$ crystal	573–883	[72]
CuInSe$_2$ thin film	763–823	[78]
Passivated CuInSe$_2$	Room temperature	[10]
CuInSe$_2$ powder in a closed capillary	673–1023	This work

at the CuInSe$_2$/In$_2$O$_3$ interface [77]; it has also been mentioned that CuInSe$_2$ evaporates during heating. In samples of thin films treated at 763–823 K, the cubic In$_2$O$_3$ phase ($a = 10.13(1)$ Å), together with a probable trace of CuO, has been found [78]. It has been noticed [79] that the intentionally deposited In$_2$O$_3$ layer on CIS causes enhancement of CIS photosensitivity. High-power laser annealing of CuInSe$_2$ also leads to formation of a In$_2$O$_3$ ($Ia\bar{3}$ space group) impurity phase [80, 81]). Formation of In$_2$Cu and In$_2$O$_3$ in a thin film has been reported in [82]. As mentioned in Sect. 1, one of the products of passivation at room temperature is the ultrathin indium oxide [10].

The occurrence range of the indium oxide impurity phase in this study can be compared with the above-mentioned observations (see Table 5). The oxide in the present study was formed at a temperature higher than those reported in the literature. The possible reasons include the nonequilibrium formation conditions (there was a relatively fast temperature increase, after a jump of 50 K each step lasting for 20 min) and inaccessibility of external air (only a small amount of air present in the closed capillary took part in the oxidation process).

The run of $a(T)$ for In$_2$O$_3$ (Fig. 3) shows that, judging after the difference with respect to literature data (nonlinear behavior at about 700–800 K), at the early stage of oxide formation in our sample, its lattice parameter is slightly higher than that expected on the basis of results of [67]. The possible reasons include off-stoichiometry, non-ideal composition at early stages of formation (impurity such as Se), strain and crystallite size effect (crystallite size for this impurity phase of our sample is the smallest at these temperatures, namely of 15–20 nm, see Fig. 4).

3.3 Lattice-parameter variation with temperature

The lattice parameters vary with temperature in a smooth way. Moreover, perfect matching of the LT and HT datasets is observed (cf. Fig. 5). The relative change of a, c, η and V in the range 11–1,073 K is about 1.0, 0.8, 0.3 and

3 %, respectively. In order to describe the temperature dependencies of the lattice parameters, these dependencies were approximated using a function of general formula:

$$y = \sum_{k=-1}^{n} a_k x^k \tag{4}$$

with $y(T)$ representing the lattice parameters and fitting coefficients defined and quoted in Table 6.

In the experimental dependencies, shallow lattice parameter minima in $a(T)$, $c(T)$ and $V(T)$ are visible (the exact values obtained from the fitting functions are 46.9, 47.0 and 46.3 K, respectively). The minimum for $c(T)$ is the least pronounced. According to the present data, the minima in the $a(T)$ and $c(T)$ run occur at the same temperature of $\sim$47 K. This is different from earlier findings [27] that they differ by about 20 K. The occurrence of the minima means that the thermal expansion of CIS becomes negative below the value of 47 K. Due to the intentionally large density of experimental points, the (weak) TEC negativity is revealed with a large degree of certainty. The reduced axial ratio forms a curve of a monotonic character that could be fitted by a simple polynomial.

The lattice-parameter variation shows the behavior observed before for smaller temperature ranges by other teams. Discrepancies with the cited data concern the absolute values of lattice parameters. In particular, the present lattice-parameter values are found to be higher in the a direction and lower in the c direction than those reported in [27]. Moreover, slopes of the $a(T)$ and $c(T)$ runs are different at the lowest temperatures. As for the HT region, the best agreement of the obtained dependencies is observed with the data of Kistaiah et al. [26], and then with those of Bodnar and Orlova [28].

The reduced axial ratio, η, varies smoothly from 1.0050 near $T = 0$ K to about 1.0022 at 1,073 K. The x coordinate of the selenium atom tends to be constant in the 300–800 K range (in agreement with earlier results presented in Fig. 5e), above this temperature a slight increase is observed. For a closely related compound, a Ga-doped CIS, a slight decrease from about 0.22 to 0.205 in the 1.5–300 K temperature range has been reported [19].

3.4 Thermal expansion

The TEC defined as

$$f(T) = (dy/dT)/y(T) \tag{5}$$

was derived from the expressions presented in the first column of Table 6 for lattice parameters, reduced axial ratio and cell volume; the derived equations are given in col. 2 of the Table. The expansion data from the LT and HT fitting function ranges were merged. All experimental
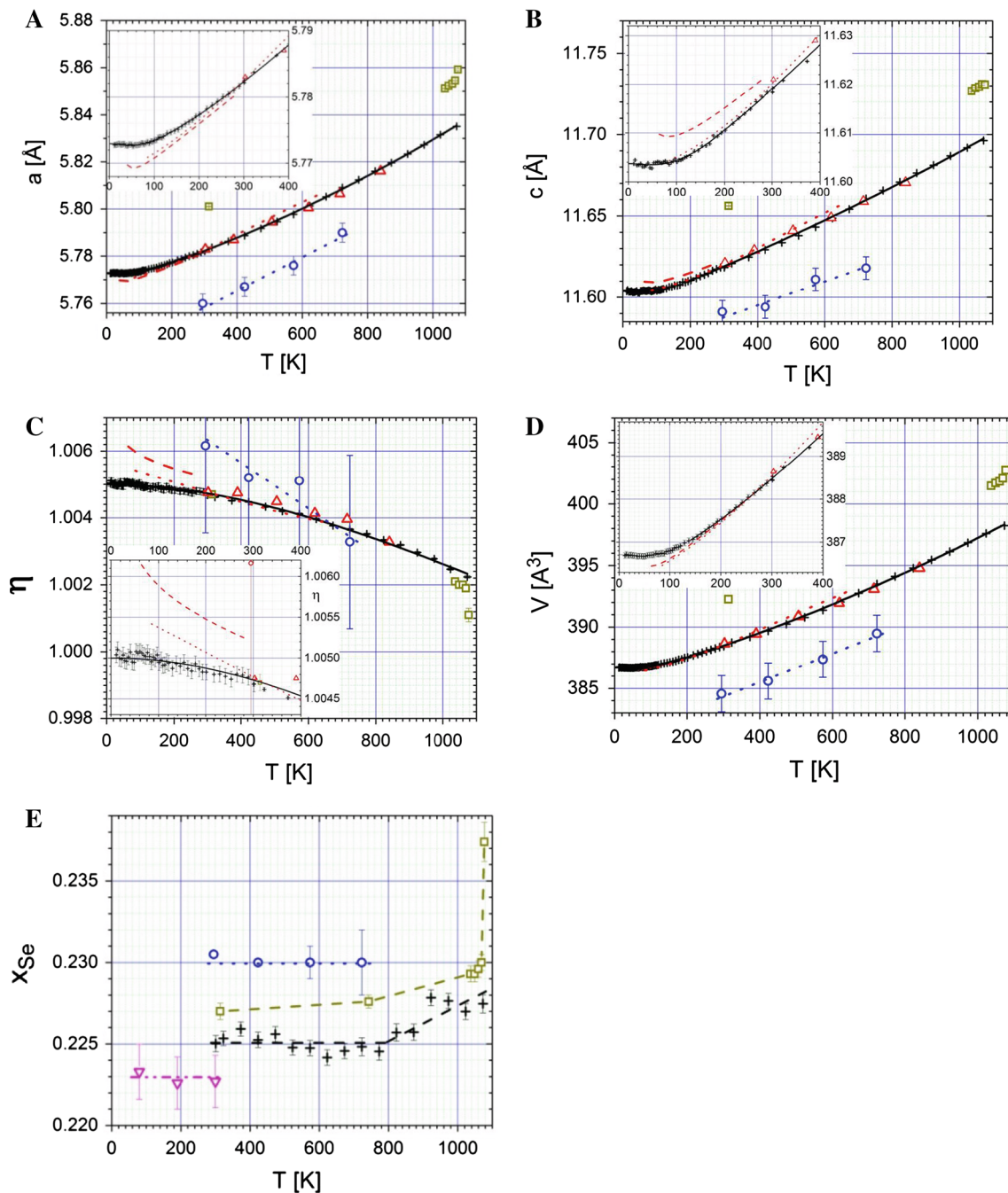
Fig. 5 Temperature dependence of the structural parameters of CuInSe₂: lattice parameter a (**a**), lattice parameter c (**b**), reduced axial ratio $\eta = c/2a$ (**c**), x_{Se} (**d**), unit cell volume V (**e**). Present results (*cross symbols*), [26] (*open triangles*), [27] (*dashed lines*), [29] (*open circles*), [23] (*filled squares*). *Dotted lines* are based on results of Bodnar and Orlova [28]. Data for nonstoichiometric CIS [17] are included in **e** (*open inverted triangles*). *Solid lines* represent the fits of the function defined in Eq. (4) with coefficients defined in Table 6, except those for x_{Se} being guide-to-the-eye *straight lines*. The uncertainties are provided where available

α_a, α_c α $_\eta$, α_V, curves are presented in Fig. 6. The experimental values of room-temperature TEC are in qualitative agreement with literature data (cf. Table 7 for the experimental values [23, 26–28, 83–87] and Table 8 for the theoretical values [31–33, 88, 89]). The TEC, α_a, α_c α_V, attain their lowest values at about 21 K (the values

resulting from the fitting curves are 20.7, 21.8 and 20.5 K, respectively). For the temperature dependence of TEC, we observe discrepancies between the present data and the data of [27, 28] (Fig. 6). The comparison with the theoretical-calculation results from [33] shows only a qualitative agreement: the cited paper reports TEC of more than

Table 6 Temperature dependence of the unit cell dimensions: approximation using the function defined by Eq. (4)

Unit cell size	Thermal expansion coefficient	Function coefficients	Temperature range (K)
$a(T) = a_0 + a_2 \times T^2 + a_3 \times T^3 + a_4 \times T^4 + a_5 \times T^5 + a_6 \times T^6 + a_7 \times T^7$	$\alpha_a = (2a_2 \times T + 3a_3 \times T^2 + 4a_4 \times T^3 + 5a_5 \times T^4 + 6a_6 \times T^5 + 7a_7 \times T^6)/a(T)$	$a_0 = 5.772956$, $a_2 = -4.035952 \times 10^{-7}$, $a_3 = 8.583646 \times 10^{-9}$, $a_4 = -5.586823 \times 10^{-11}$, $a_5 = 1.780271 \times 10^{-13}$, $a_6 = -2.79837519 \times 10^{-16}$, $a_7 = 1.72945332 \times 10^{-19}$	$0 < T \leq 184.5$
$a(T) = a_{-1} \times T^{-1} + a_0 + a_1 \times T + a_2 \times T^2 + a_3 \times T^3$	$\alpha_a = (-a_{-1} \times T^{-2} + a_1 + 2a_2 \times T + 3a_3 \times T^2)/a(T)$	$a_{-1} = 0.2367847$, $a_0 = 5.766470$, $a_1 = 4.457229 \times 10^{-5}$, $a_2 = 1.844636 \times 10^{-8}$, $a_3 = -2.559021 \times 10^{-13}$	$184.5 < T \leq 1,073$
$c(T) = a_0 + a_2 \times T^2 + a_3 \times T^3 + a_4 \times T^4 + a_5 \times T^5 + a_6 \times T^6$	$\alpha_c = (2a_2 \times T + 3a_3 \times T^2 + 4a_4 \times T^3 + 5a_5 \times T^4 + 6a_6 \times T^5)/c(T)$	$a_0 = 11.603711$, $a_2 = -3.2193676 \times 10^{-7}$, $a_3 = 6.0305159 \times 10^{-9}$, $a_4 = -2.6093451 \times 10^{-11}$, $a_5 = 4.7714458 \times 10^{-14}$, $a_6 = -3.2124118 \times 10^{-17}$	$0 < T \leq 182.5$
$c(T) = a_{-1} \times T^{-1} + a_0 + a_1 \times T + a_2 \times T^2 + a_3 \times T^3$	$\alpha_c = (-a_{-1} \times T^{-2} + a_1 + 2a_2 \times T + 3a_3 \times T^2)/c(T)$	$a_{-1} = 0.540082$, $a_0 = 11.589640$, $a_1 = 8.993863 \times 10^{-5}$, $a_2 = 6.189999 \times 10^{-9}$, $a_3 = 2.983710 \times 10^{-12}$	$182.5 < T \leq 1,073$
$\eta(T) = a_0 + a_1 \times T + a_2 \times T^2 + a_3 \times T^3$	$\alpha_\eta = (a_1 + 2a_2 \times T + 3a_3 \times T^2)/\eta(T)$	$a_0 = 1.0049993$, $a_2 = -3.23841500 \times 10^{-9}$, $a_3 = 8.56641328 \times 10^{-13}$	$0 < T \leq 1,073$
$V(T) = a_0 + a_2 \times T^2 + a_3 \times T^3 + a_4 \times T^4 + a_5 \times T^5 + a_6 \times T^6 + a_7 \times T^7$	$\alpha_V = (2a_2 \times T + 3a_3 \times T^2 + 4a_4 \times T^3 + 5a_5 \times T^4 + 6a_6 \times T^5 + 7a_7 \times T^6)/V(T)$	$a_0 = 386.71326$, $a_2 = -5.797420 \times 10^{-5}$, $a_3 = 1.21662 \times 10^{-6}$, $a_4 = -7.358308 \times 10^{-9}$, $a_5 = 2.197162 \times 10^{-11}$, $a_6 = -3.282617 \times 10^{-14}$, $a_7 = 1.9537151 \times 10^{-17}$	$0 < T \leq 145.5$
$V(T) = a_{-1} \times T^{-1} + a_0 + a_1 \times T + a_2 \times T^2 + a_3 \times T^3$	$\alpha_V = (-a_{-1} \times T^{-2} + a_1 + 2a_2 \times T + 3a_3 \times T^2)/V(T)$	$a_{-1} = 49.33478$, $a_0 = 385.38611$, $a_1 = 8.926931 \times 10^{-3}$, $a_2 = 2.771685 \times 10^{-6}$, $a_3 = 9.971967 \times 10^{-11}$	$145.5 < T \leq 1,073$

Table 7 Experimental thermal expansion coefficients of CuInSe₂

α_a (MK^{-1})	α_c (MK^{-1})	$\alpha_V/3$ (MK^{-1})	$\alpha_{c/2a}$	Material studied	Temperature range (K)	Ref.
11.4	8.6	10.5			>300	[83]
6.4	5.0	5.9	−1.55		80–174	[84]
11.0	8.4	10.1	−2.6		300–573	[84]
10.32	7.89	9.51	−2.41	Powdered single crystal	301–839	[26]
−1.3 to 9.6 (2)	−1.8 to 6.4 (8)	**≤8.53**		Single crystal	40–285 [83], 60–285 [26]	[27]
11.2	7.9	10.1	−3.3	Polycrystal	RT	[28]
10.8	7.7	9.8			293–713	[85]
		9.15			293	[86]
		10.12		Single crystals	RT	[87]
		7.951–9.957		Polycrystal	315–1,060	[23]
9.15	7.61	8.62	−1.71	Powdered single crystal	300	This work

Value of the linear expansion coefficient is defined as ($\alpha_L = \alpha_V/3$). The bold values refer to broader ranges of temperature

Table 8 Theoretical thermal expansion coefficients of CuInSe₂

α_a (MK^{-1})	α_c (MK^{-1})	$\alpha_V/3$ (MK^{-1})	Temperature range (K)	Method	Ref.
10.6	7.9	9.7		Theoretical (estimation)	[31]
6.8	8.5	7.37	RT	Prediction	[32]
		9.81	RT	Calculated	[88]
		27	30–300	Calculated	[33]
		7.54	RT	Calculated	[89]

is monotonic, but these trends are in opposite directions: values of (α_a, α_c) pairs for these three chalcopyrites) are (13.4 MK^{-1}, 4.6 MK^{-1}), (13.1 MK^{-1}, 5.2 MK^{-1}), and (11.2 MK^{-1}, 8.4 MK^{-1}), respectively. The present result documents the smaller values of the last pair, but the reported trend is conserved.

4 Summary

In this paper, structural and elastic properties of powdered chalcopyrite-type CuInSe₂ crystal prepared from a slowly cooled melt are studied. For the first time, the lattice parameters and TEC are experimentally determined in a broad range ($11 \leq T \leq 1,073$ K) by X-ray diffraction, using a synchrotron-radiation source; so an almost complete stability range of this compound is now covered.

The temperature dependencies of the TEC are derived and discussed on the basis of the existing literature. The low- and high-temperature experimental thermal expansion data are found to follow the trends previously reported for narrow temperature ranges. According to the present results, the TEC values at 300 K are $\alpha_a = 9.15$ MK^{-1}, $\alpha_c = 7.61$ MK^{-1}, $\alpha_V/3 = 8.62$ MK^{-1}, $\alpha_\eta = 1.71$ MK^{-1}. Our results, based on fitting of a large number of points, provide the data on thermal expansion anisotropy and give an experimental evidence that below 47 K the linear expansion coefficient is negative in both a and c directions. In the c direction, the negativity obtained by fitting is less pronounced than that in the a direction. The temperature at which thermal expansion changes the sign is in between the previously reported theoretical value of 35 K and the experimental ones of 60 and 80 K. The obtained results also show how the thermal expansion anisotropy decreases with rising temperature.
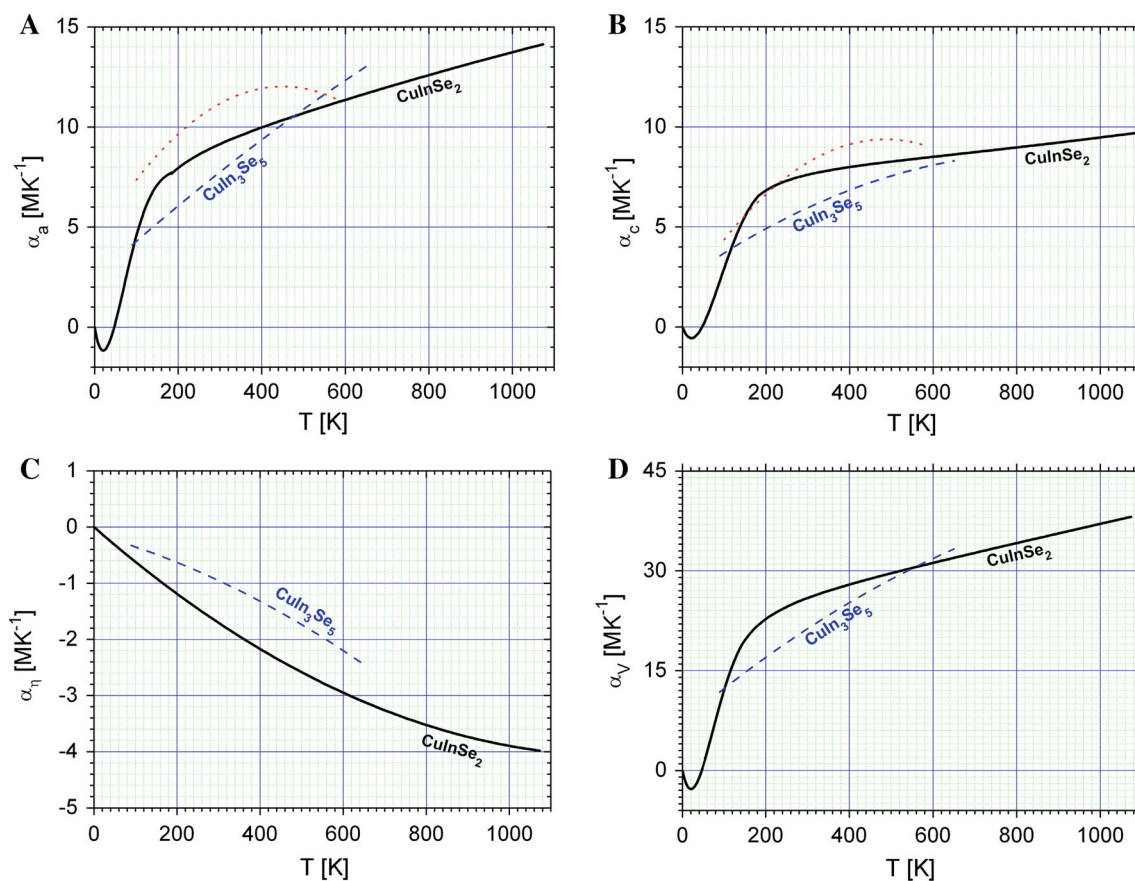
two times higher magnitude, but the temperature for the change of sign is not much different than in our experiment (35 versus 47 K) and the vanishing of the thermal expansion at the lowest temperatures is confirmed.

The present study allows for creation of a reliable image of the CuInSe₂ thermal expansion anisotropy: generally the expansion is markedly larger in the [100] direction than in the [001] direction. In particular, the present results provide, for room temperature, smaller values of α_a, α_c (9.15, 7.61 MK^{-1}, respectively), than most of those quoted in Table 7.

A comparison to data for a chemically related CuIn₃Se₅ shows that for CIS the magnitude of thermal expansion tends to be larger (in the common range), the expansion anisotropy is also more pronounced than that of the CuIn₃Se₅ compound [90], as is illustrated in Fig. 6c.

As noticed in [31–33, 84, 91], various chalcopyrite-type A^{I}B^{II}C$_2^{VI}$ compounds exhibit a large TEC anisotropy manifested by larger TEC values for the [100] direction than that for the [001] direction. The room-temperature thermal expansion of chalcopyrite-type materials has been reviewed in [32]: they are characterized by a considerable TEC, especially for A = Zn, Cd; for CIS, the anisotropy is somewhat less pronounced. Interestingly, along the CuXSe₂ series (X = Al, Ga, In), the variation of both α_a and α_c at RT

Fig. 6 Thermal expansion coefficients, α_a, α_c, α_η and α_V, of CuInSe$_2$ as a function of temperature, as derived from the fitted temperature dependencies given in Table 6. The y scales for **a**, **b**, **d** were selected to enable easy comparison of absolute values. *Dotted lines* in **a** and **b** are based on the data of [28] for CuInSe$_2$. The literature data for CuIn$_3$Se$_5$ [90] (*dashed lines*) are shown for comparison

Indium oxide was experimentally observed in trace amount at high temperatures of 673–1,023 K as an impurity phase, formed through reaction with air closed in the sealed capillary. Its presence and properties are briefly discussed; the present range is comparable with that of one of earlier studies (573–883 K) and the In$_2$O$_3$ lattice-parameter variation with temperature agrees with literature data for a bulk polycrystalline material.

References

1. T. Gödecke, T. Haalboom, F. Ernst, Phase equilibria of Cu-In-Se. I. Stable states and nonequilibrium states of the In$_2$Se$_3$–Cu$_2$Se subsystem. Z. Metallkd. **91**(8), 622–634 (2000)
2. T. Wada, S. Nakamura, T. Maeda, Ternary and multinary Cu chalcogenide photovoltaic materials from CuInSe$_2$ to Cu$_2$ZnSnS$_4$ and other compounds. Prog. Photovolt. Res. Appl. **20**, 520–525 (2012)
3. B.J. Stanbery, Copper indium selenides and related materials for photovoltaic devices. Crit. Rev. Solid State Mater. Sci. **27**(2), 73–117 (2002)
4. J.R. Tuttle, J.S. Ward, A. Duda, T.A. Berens, M.A. Contreras, K.R. Ramanathan, A.L. Tennant, J. Keane, E.D. Cole, K. Emery, R. Noufi, The performance of Cu(In,Ga)Se$_2$-based solar cells in conventional and concentrator applications. Mater. Res. Soc. Symp. Proc. **426**, 143–152 (1996)
5. A. Goetzberger, C. Hebling, H.W. Schock, Photovoltaic materials, history, status and outlook. Mater. Sci. Eng. R **40**(1), 1–46 (2003)
6. M.A. Contreras, K. Ramanathan, J. AbuShama, F. Hasoon, D.L. Young, B. Egaas, R. Noufi, Diode characteristics in state-of-the-art ZnO/CdS/Cu(In$_{1-x}$Ga$_x$)Se$_2$ solar cells. Prog. Photovolt. Res. Appl. **13**, 209–216 (2005)
7. I. Repins, M.A. Contreras, B. Egaas, C. DeHart, J. Scharf, C.L. Perkins, B. To, R. Noufi, 19.9 %-efficient ZnO/CdS/CuInGaSe$_2$ solar cell with 81.2 % fill factor. Prog. Photovolt. Res. Appl. **16**, 235–239 (2008)
8. L.S. Hamideche, A. Amara, M. Mekhnache, O. Kamli, A. Benaldjia, A. Drici, J.C. Bernede, M. Guerioune, N. Benslim, L. Bechiri, Nanostructured thermally evaporated CuInSe$_2$ thin films synthesized from mechanically alloyed powders and self-combustion ingot. Mater. Sci. Semicond. Proc. **15**, 145–151 (2012)
9. A. Rockett, R.W. Birkmire, CuInSe$_2$ for photovoltaic applications. J. Appl. Phys. **70**(7), R81–R97 (1991)
10. D. Regesch, L. Gütay, J.K. Larsen, V. Deprédurand, D. Tanaka, Y. Aida, S. Siebentritt, Degradation and passivation of CuInSe$_2$. Appl. Phys. Lett. **101**, 112108–1–4 (2012)

11. S. Wagner, J.L. Shay, P. Migliorato, H.M. Kasper, CuInSe$_2$/CdS heterojunction photovoltaic detectors. Appl. Phys. Lett. **25**, 434–435 (1974)

12. L. Chernyak, A. Jakubowicz, D. Cahen, Junction electroluminescence from microscopic diode structures in CuInSe$_2$, prepared by electric field-assisted doping. Adv. Mater. **7**, 45–48 (1995)

13. J.-J. Wang, Y.-Q. Wang, F–.F. Cao, Y.-G. Guo, L.-J. Wan, Synthesis of monodispersed wurtzite structure CuInSe$_2$ nanocrystals and their application in high-performance organic–inorganic hybrid photodetectors. J. Am. Chem. Soc. **132**(35), 12218–12221 (2010)

14. U.-C. Boehnke, G. Kuhn, Phase relations in the ternary system Cu–In–Se. J. Mater. Sci. **22**, 1635–1641 (1987)

15. J.M. Merino, J.L. Martín de Vidales, S. Mahanty, R. Díaz, F. Rueda, M. León, Composition effects on the crystal structure of CuInSe$_2$. J. Appl. Phys. **80**(10), 5610–5616 (1996)

16. L.I. Gladkikh, E.I. Rogacheva, T.V. Tavrina, L.P. Fomina, X-ray diffraction study of nonstoichiometry in CuInSe$_{2+d}$, Inorganic Materials (Russia) **36**(11), 1098–1100 (2000) [transl. from: Izv. Akad. Nauk, Neorg. Mater. **36**(11), 1309–1312 (2000)]

17. G. Zahn, P. Paufler, Identification of predominant point defects in nonstoichiometric CuInSe$_2$ by X-ray powder diffraction. Cryst. Res. Technol. **23**(4), 499–507 (1988)

18. C. Stephan, S. Schorr, H.-W. Schock, New structural investigations in the Cu$_2$Se(S)–In$_2$Se(S)$_3$/Cu$_2$Se(S)–Ga$_2$Se(S)$_3$ phase diagram. Mater. Res. Soc. Symp. **1165**, 411–417 (2011)

19. C. Stephan, Structural trends in off-stoichiometric chalcopyrite type compound semiconductors. Dissertation, Institut für Technologie, Freie Universität Berlin, 2011

20. L. Gütay, D. Regesch, J.K. Larsen, Y. Aida, V. Deprédurand, A. Redinger, S. Caneva, S. Schorr, C. Stephan, J. Vidal, S. Botti, S. Siebentritt, Feedback mechanism for the stability of the band gap of CuInSe$_2$. Phys. Rev. B **86**, 045216–1–5 (2012)

21. A. Zunger, S.B. Zhang, S.-H. Wei, Revisiting the defect physics in CuInSe$_2$ and CuGaSe$_2$. Conference record of the twenty sixth IEEE photovoltaic specialists conference (IEEE, 1997), pp. 313–318

22. H. Neumann, J. Łażewski, P.T. Jochym, K. Parlinski, Ab initio heat capacity and atomic temperature factors of chalcopyrites. Phys. Rev. B **75**, 224301–1–7 (2007)

23. S. Schorr, G. Geandier, In-situ investigation of the temperature dependent structural phase transition in CuInSe$_2$ by synchrotron radiation. Cryst. Res. Technol. **41**(5), 450–457 (2006)

24. T. Wada, N. Kohara, T. Negami, M. Nishitani, Growth of CuInSe$_2$ crystals in Cu-rich Cu–In–Se thin films. J. Mater. Res. **12**(6), 1456–1462 (1997)

25. M.E. Norako, R.L. Brutchey, Synthesis of metastable wurtzite CuInSe$_2$ nanocrystals. Chem. Mater. **22**(5), 1613–1615 (2010)

26. P. Kistaiah, Y.C. Venudhar, K.S. Murthy, L. Iyengart, K.V. Krishna Rao, Temperature dependence of tetragonal distortion and thermal expansion of copper indium selenide. J. Phys. D Appl. Phys. **14**, 1311–1316 (1981)

27. P. Deus, H. Neumann, G. Kuhn, B. Hinze, Low-temperature thermal expansion in CuInSe$_2$. Phys. Status Solidi (a) **80**, 205–209 (1983)

28. I.V. Bodnar, N.S. Orlova, Thermal expansion of CuAlSe$_2$, CuGaSe$_2$, CuInSe$_2$. Inorg. Mater. **21**, 967–970 (1985); [transl. from Izv. Akad. Nauk SSSR, Neorg. Mater. **21**, 1110–1113 (1985)]

29. M.Kh. Rabadanov, I.A. Verin, X-ray diffraction study of CuInSe$_2$ single crystals. Inorg. Mater. **34**(1), 14–16 1998; [transl. from Neorg. Mater. **34**(1), 20–23 (1998)]

30. H. Neumann, Lattice vibrational, thermal and mechanical properties of CuInSe$_2$. Solar Cells **16**, 399–418 (1986)

31. H. Neumann, Trends in the thermal expansion coefficients of the A^{I}B^{III}C$_2^{VI}$ and A^{II}B^{IV}C$_2^{V}$ chalcopyrite compounds. Krist. Technik **15**(7), 849–857 (1980)

32. G.C. Bhar, L.K. Samanta, Some structural correlations in chalcopyrite crystals. Phys. Rev. B **26**(4), 2275–2279 (1982)

33. S.V. Ponomarev, K.G. Nikiforov, Modeling of anisotropic thermal expansion of anisotropic multicomponent I–III–V$_2$ semiconductors of chalcopyrite structure. Issledovano v Rossii **10**, 1996–2003 (2007). (in Russian)

34. A. Wolska, R. Bacewicz, J. Filipowicz, K. Attenkofer, X-ray absorption near-edge structure of selenium in the Cu–In–Se system. J. Phys.: Condens. Matter **13**, 4457–4470 (2001)

35. R. Lewandowska, R. Bacewicz, J. Filipowicz, EXAFS study of in-rich phases in Cu–In–Se system. Cryst. Res. Technol. **37**, 235–241 (2002)

36. M. Knapp, C. Baehtz, H. Ehrenberg, H. Fuess, The synchrotron powder diffractometer at beamline B2 at HASYLAB/DESY: status and capabilities. J. Synchrotron Radiat. **11**, 328–334 (2004)

37. M. Knapp, V. Joco, C. Baehtz, H.H. Brecht, A. Berghaeuser, H. Ehrenberg, H. von Seggern, H. Fuess, Position-sensitive detector system OBI for high resolution x-ray powder diffraction using on-site readable image plates. Nucl. Instrum. Methods A **521**, 565–570 (2004)

38. W. Paszkowicz, M. Knapp, C. Baehtz, R. Minikayev, P. Piszora, J.Z. Jiang, R. Bacewicz, Synchrotron X-ray wavelength calibration using a diamond internal standard: application to low-temperature thermal-expansion studies. J. Alloy. Compd. **382**, 107–111 (2004)

39. W. Paszkowicz, R. Minikayev, P. Piszora, M. Knapp, C. Bähtz, J.M. Recio, M. Marqués, P. Mori-Sánchez, L. Gerward, J.Z. Jiang, Thermal expansion of spinel-type Si$_3$N$_4$. Phys. Rev. B **69**, 052103–1–4 (2004)

40. T. Sato, K. Ohashi, T. Sudoh, K. Haruna, H. Maeta, Thermal expansion of a high purity synthetic diamond single crystal at low temperatures. Phys. Rev. B **65**, 092102–1–4 (2002)

41. R.R. Reeber, K. Wang, Thermal expansion, molar volume and specific heat of diamond from 0 to 3000 K. J. Electron. Mater. **25**(1), 63–67 (1996)

42. J. Rodriguez-Carvajal, FULLPROF: a program for Rietveld refinement and pattern matching analysis. Abstracts of the satellite meeting on powder diffraction of the XV congress of the IUCr, p. 127, Toulouse (1990)

43. K. Nagata, Y. Miyamoto, K. Takarabe, Refinement of the crystal structure of CuInSe$_2$. Fukuoka Daigaku Rigaku Shuho **19**(2), 103–107 (1989)

44. H. Kitahara, K. Suda, N. Ishizawa, A CCD camera system for X-ray diffraction studies of single crystals. Rep. Res. Lab. Eng. Mater. Tohoku Inst. Technol. **21**, 1–19 (1996)

45. V. Lyahovitskaya, S. Richter, F. Frolow, L. Kaplan, Y. Manassen, K. Gartsman, D. Cahen, Growth of single CuInSe$_2$ crystals by the traveling heater method and their characterization. J. Cryst. Growth **197**, 177–185 (1999)

46. L. Kaplan, G. Leitus, V. Lyakhovitskaya, F. Frolow, H. Hallak, Å. Kvick, D. Cahen, Synchrotron X-ray diffraction evidence for native defects in the photovoltaic semiconductor CuInSe$_2$. Adv. Mater. **12**, 366–377 (2000)

47. J.M. Merino, M. Di Michiel, M. Leon, Structural analysis of CuInSe$_2$ and CuIn$_3$Se$_5$ at different temperatures with synchrotron radiation. J. Phys. Chem. Solids **64**, 1649–1652 (2003)

48. W. Paszkowicz, R. Lewandowska, R. Bacewicz, Rietveld refinement for CuInSe$_2$ and CuIn$_3$Se$_5$. J. Alloy. Compd. **362**, 241–247 (2004)

49. M. León, J.M. Merino, G. Van Tendeloo, Structural analysis of CuInSe$_2$, CuInTe$_2$ and CuInSeTe by electron microscopy and X-ray techniques. Acta Microscópica **18**(2), 128–138 (2009)

50. J. Yao, C.N. Kline, H. Gu, M. Yan, J.A. Aitken, Effects of Mn substitution on the structure and properties of chalcopyrite-type CuInSe$_2$. J. Solid State Chem. **182**, 2579–2586 (2009)

51. M. Souilah, A. Lafond, C. Guillot-Deudon, S. Harel, M. Evain, Structural investigation of the Cu_2Se–In_2Se_3–Ga_2Se_3 phase diagram, X-ray photoemission and optical properties of the $Cu_{1-z}(In_{0.5}Ga_{0.5})_{1+z/3}Se_2$ compounds. J. Solid State Chem. **183**, 2274–2280 (2010)

52. J. Yao, Z. Wang, J. van Tol, N.S. Dalal, J.A. Aitken, Site preference of manganese on the copper site in Mn-substituted $CuInSe_2$ chalcopyrites revealed by a combined neutron and X-ray powder diffraction study. Chem. Mater. **22**, 1647–1655 (2010)

53. J. Yao, C.D. Brunetta, J.A. Aitken, Suppression of antiferromagnetic interactions through Cu vacancies in Mn-substituted $CuInSe_2$ chalcopyrites. J. Phys.: Condens. Matter **24**, 086006-1-6 (2012)

54. W. Paszkowicz, P. Piszora, R. Minikayev, M. Knapp, Unpublished (2001)

55. J. Parkes, R.D. Tomlinson, M.J. Hampshire, Crystal data for $CuInSe_2$. J. Appl. Crystallogr. **6**, 414–416 (1973)

56. A. Baldus, K.W. Benz, Melt and metallic solution crystal growth of $CuInSe_2$. J. Cryst. Growth **130**(1–2), 37–44 (1993)

57. K.S. Knight, The crystal structures of $CuInSe_2$ and $CuInTe_2$. Mater. Res. Bull. **27**, 161–167 (1992)

58. T. Matsuoka, Y. Nagahori, S. Endo, Preparation and characterization of electrodeposited $CuGa_xIn_{1-x}Se_2$ thin films. J. Appl. Phys. **33**(11), 6105–6110 (1994)

59. T. Wada, H. Kinoshita, S. Kawata, Preparation of chalcopyrite-type $CuInSe_2$ by non-heating process. Thin Solid Films **431–432**(1), 1–15 (2003)

60. H. Zhong, Y. Li, M. Ye, Z. Zhu, Y. Zhou, C. Yang, A facile route to synthesize chalcopyrite $CuInSe_2$ nanocrystals in non-coordinating solvent. Nanotechnology **18**(2), 485–489 (2007)

61. Q. Guo, S.J. Kim, M. Kar, W.N. Shafarman, R.W. Birkmire, E.A. Stach, R. Agrawal, H.W. Hillhouse, Development of $CuInSe_2$ nanocrystal and nanoring inks for low-cost solar cells. Nano Lett. **8**(9), 2982–2987 (2008)

62. M.R. Balboul, H.W. Schock, S.A. Fayak, A. Abdel El-Aal, J.H. Werner, A.A. Ramadan, Correlation of structure parameters of absorber layer with efficiency of $Cu(In,Ga)Se_2$ solar cell. Appl. Phys. A Mater. Sci. Process. **92**, 557–563 (2008)

63. S. Mehdaoui, N. Benslim, O. Aissaoui, M. Benabdeslem, L. Bechiri, A. Otmani, X. Portier, G. Nouet, Study of the properties of $CuInSe_2$ materials prepared from nanoparticle powder. Mater. Charact. **60**(5), 451–455 (2009)

64. A.V. Postnikov, M.V. Yakushev, Lattice dynamics and stability of $CuInSe_2$. Thin Solid Films **451–452**(22), 141–144 (2004)

65. S. Agilan, D. Mangalaraj, S.K. Narayandass, S. Velumani, A. Ignatiev, Structural and optical characterization of $CuInSe_2$ films deposited by hot wall vacuum evaporation method. Vacuum **81**, 813–818 (2007)

66. F. Frolow, L. Chernyak, D. Cahen, H. Hallak, J. Gabboun, Å. Kvick, H. Graafsma, Single crystal synchrotron X-ray diffraction of $CuInSe_2$. Inst. Phys. Conf. Ser. **152**, 67–70 (1998)

67. K.D. Kundra, S.Z. Ali, Thermal expansion of In_2O_3. J. Appl. Cryst. **3**, 543–545 (1970)

68. C.H. Lee, M. Kim, T. Kim, A. Kim, J. Paek, J.W. Lee, S.-Y. Choi, K. Kim, J.-B. Park, K. Lee, Ambient pressure syntheses of size-controlled corundum-type In_2O_3 nanocubes. J. Am. Chem. Soc. **128**(29), 9326–9327 (2006)

69. J.F. Wager, O. Jamjoum, L.L. Kazmerski, The CdS–$CuInSe_2$ solar cell interface: thermodynamic considerations. Solar Cells **9**, 159–168 (1983)

70. R. Brini, M. Kanzari, B. Rezig, J. Werckmann, Effect of annealing on properties of $CuInS_2$ thin films. Eur. Phys. J. Appl. Phys. **30**, 153–158 (2005)

71. L.L. Kazmerski, O. Jamjoum, J.F. Wager, P.J. Ireland, K.J. Bachmann, Oxidation of $CuInSe_2$. J. Vac. Sci. Technol., A **1**, 668–669 (1983)

72. G.A. Medvedkin, R.N. Bekimbetov, T.L. Makarova, A.D. Smirnova, V.I. Sokolova, Optical properties of a thermal oxide on $CuInSe_2$. Zh. Tekhn. Fiz. **57**, 960–964 (1987). In Russian

73. N. Khare, G. Razzinia, L. Peraldo Bicellia, Electrodeposition and heat treatment of $CuInSe_2$ films. Thin Solid Films **186**, 113–128 (1990)

74. H. Sobotta, H. Neumann, R.D. Tomlinson, V. Riede, Infrared optical characterization of thermally oxidized $CuInSe_2$ single crystals. Cryst. Res. Technol. **26**(4), 485–489 (1991)

75. E.P. Zaretskaya, V.F. Gremenok, I.A. Viktorov, I.V. Bodnar, $CuInSe_2$ films laser-evaporated in an oxygen atmosphere. J. Appl. Spectrosc. **61**(5–6), 785–789 (1994)

76. L.L. Kazmerski, P.J. Ireland, O. Jamjoum, S.K. Deb, P. Sheldon, R.A. Mickelsen, W. Chen, K. Bachmann, Oxidation-stability studies of $CuInSe_2$, In: 15th photovoltaic specialists conference, Kissimmee, pp. 12–15 (1981). Abstracts http://adsabs.harvard.edu/abs/1981pvsp.conf.24

77. G. Matuschek, A. Finke, W. Thumm, A. Kettrup, Thermal investigations of active compounds in thin-layer photovoltaic modules (CdTe and $CuInSe_2$). Thermochim. Acta **263**, 23–28 (1995)

78. M.E. Boiko, G.A. Medvedkin, Thermal oxidation of $CuInSe_2$, experiment and physico-chemical model. Solar Energy Mater. Solar Cells **41**(42), 307–314 (1996)

79. M.A. Abdullaev, I.K. Kamillov, D.Kh. Magomedova, G.B. Makatova, P.P. Khokhlachev, Effects of the preparation procedure and In_2O_3 thickness on the electrical and photovoltaic properties of In_2O_3/$CuInSe_2$ heterostructures. Inorg. Mater. **40**(11), 1181–1185 (2004); transl. from Neorg. Mater. **40**(11), 1345–1349 (2004)

80. S. Jost, R. Schurr, F. Hergert, R. Hock, J. Schulze, A. Kirbs, T. Voß, M. Purwins, J. Palm, I. Mys, The formation of $CuInSe_2$ thin-film solar cell absorbers by laser annealing of electrodeposited precursors. Solar Energy Mater. Solar Cells **92**, 410–417 (2008)

81. S. Jost, The formation of $CuInSe_2$-based thin-film solar cell absorbers from alternative low-cost precursors, PhD thesis (Den Naturwissenschaftlichen Fakultäten der Friedrich-Alexander-Universität Erlangen-Nürnberg 2008)

82. S.-H. Liu, F.-S. Chen, C.-H. Lu, Preparation of thin $CuInSe_2$ films using Cu–In alloy nanoparticles. Chem. Lett. **39**(12), 1333–1335 (2010)

83. H. Haupt, K. Hess, Growth of large $CuInSe_2$ single crystal. Inst. Phys. Conf. Ser. **35**(5), 5–12 (1977)

84. H.-G. Brühl, H. Neumann, T. Pfeiffer, G. Kühn, Anisotropic thermal expansion of Cu–III–VI_2 compounds. Phys. Status Solidi (a) **66**(2), 597–600 (1981)

85. R.D. Tomlinson, Fabrication of $CuInSe_2$ single crystals using melt-growth techniques. Solar Cells **16**, 17–26 (1986)

86. I.V. Bodnar, B.V. Korzun, L.V. Chibusova, Temperature dependence of the thermal expansion coefficient of $(CuInSe_2)_{1-x}(2ZnSe)_x$ solid solutions. Phys. Status Solidi (a) **174**(1), 199–203 (1999)

87. N.S. Orlova, I.V. Bodnar', T.L. Kushner, O.E. Andreeva, Characteristics of interatomic interactions in $CuIn_3Se_5$, $CuGa_3Se_5$ and $CuGa_5Se_8$. In: Proceedings of the International Conference on Solid State Physics, vol. 2, Minsk 2005, pp. 354–366 (in Russian)

88. V. Kumar, B.S.R. Sastry, Relationship between the thermal expansion coefficient, plasmon energy, and bond length of ternary chalcopyrite semiconductors. J. Phys. Chem. Solids **63**(1), 107–112 (2002)

89. A.S. Verma, Thermal properties of chalcopyrite semiconductors. Philos. Mag. **89**(2), 183–193 (2009)

90. N.S. Orlova, I.V. Bodnar, T.L. Kushner, Structural and physical–chemical properties of the $CuGa_5Se_8$, $CuGa_3Se_5$ and $CuIn_3Se_5$ compounds. J. Phys. Chem. Solids **64**, 1895–1899 (2003)

91. H. Neumann, Thermal expansion anisotropy and individual bond expansion coefficients in ternary chalcopyrite compounds. Cryst. Res. Technol. **22**(5), 723–729 (1987)